



Cite this: *RSC Adv.*, 2021, **11**, 26928

Constructing NiSe₂@MoS₂ nano-heterostructures on a carbon fiber paper for electrocatalytic oxygen evolution

Yazhou Huang, * Jiakai Huang, Kunshan Xu and Ranran Geng

Although MoS₂ has shown its potential as an electro-catalyst for the oxygen evolution reaction (OER), its research is still insufficient. In this study, as a novel MoS₂-based heterostructure electro-catalyst for OER, namely NiSe₂@MoS₂ nano-heterostructure, was constructed on a carbon fiber paper (CFP) substrate by a simple approach, which includes electrochemical deposition of NiSe₂ film and hydrothermal processing of MoS₂ film. In addition to a series of observations on the material structure, electrocatalytic OER performance of NiSe₂@MoS₂ was fully evaluated and further compared with other MoS₂-based OER electro-catalysts. It exhibits an outstanding catalytic performance with an overpotential η_{10} of 267 mV and a Tafel slope of 85 mV dec⁻¹. Only 6% loss of current density before and after 10 h indicates its excellent durability. The results indicate that the obtained NiSe₂@MoS₂ is an excellent OER electro-catalyst and worth exploring as a substitute for noble metal-based materials.

Received 18th July 2021

Accepted 24th July 2021

DOI: 10.1039/d1ra05509g

rsc.li/rsc-advances

1. Introduction

In order to solve the contradiction between environmental protection and energy demand, exploring clean energy such as hydrogen and oxygen has attracted wide attention.¹ Among different methods, splitting water into hydrogen and oxygen by the electrochemical method possesses advantages of high efficiency and abundant water resources, and is considered to be one of the most promising methods.^{2–7} However, the application of this method is limited because the high overpotential in the oxygen evolution reaction (OER) process will lead to a significant loss of energy.⁸ Although noble metal oxides such as IrO₂ and RuO₂ are considered to be efficient catalysts for the reduction of the OER overpotential, they cannot be used on a large scale owing to their scarcity and high-cost.^{9,10} Therefore, it is of great importance to find other OER catalysts with low cost and abundant reserves, and a lot of efforts have been made in this regard.^{11–18}

Recently, as a layered material, MoS₂ has been regarded as an efficient electro-catalyst for the hydrogen evolution reaction (HER) and exhibited an excellent performance.^{19,20} However, research on its OER catalytic performance is still not sufficient. The theoretical calculation shows that the OER active sites of MoS₂ are at the edge with sulfur vacancies, which are similar to HER.²¹ According to the reports, there are two main methods to improve the OER catalytic activity of MoS₂. The first method is to increase the exposure of the active sites by reducing the grain size and increasing the substrate gap.²² However, the improvement is limited owing to the intrinsic structure of MoS₂.²³ The

second method is to improve the electronic structure of MoS₂, for example, hybridizing MoS₂ with other materials to facilitate the chemical adsorption of oxygen-containing intermediates, so as to reduce the kinetics of OER.²⁴ Recently, Co/Ni-sulfide@MoS₂ heterostructures such as Co₉S₈@MoS₂,²⁵ CoS₂-C@MoS₂,²⁶ and MoS₂/Ni₃S₂ (ref. 27) have demonstrated excellent OER activities. Compared with sulfide, the electronegativity of selenide is lower, which might weaken the chemical bond between the Se atom and the bonding electrons, and thus exhibits greater activity.^{28–31} For example, in the OER process, the Tafel slope of NiSe₂ is 97 mV dec⁻¹, which is lower than that of Ni₃S₂ (118 mV dec⁻¹).^{27,32} Therefore, it is worthwhile to construct the nanoscale Ni-selenide@MoS₂ heterostructure on a substrate with abundant gaps and high conductivity as a catalyst for OER.

In this study, a novel MoS₂-based nano-heterostructure electro-catalyst, NiSe₂@MoS₂, was constructed on a carbon fiber paper (CFP) substrate for OER by a simple method, which includes the electrochemical deposition and hydrothermal processes. Various techniques were then employed to observe the material structure. Moreover, the electrocatalytic OER performances were fully evaluated by electrochemical measurements and further compared with other MoS₂-based OER electro-catalysts.

2. Experimental

2.1. Construction of the NiSe₂@MoS₂ nano-heterostructure on CFP

As shown in Fig. 1, the construction process of the NiSe₂@MoS₂ nano-heterostructure includes two steps: electrochemical deposition of the NiSe₂ film and hydrothermal synthesis of the MoS₂ film.

Industrial Center, Nanjing Institute of Technology, Nanjing 211167, People's Republic of China. E-mail: huangyazhou@njit.edu.cn



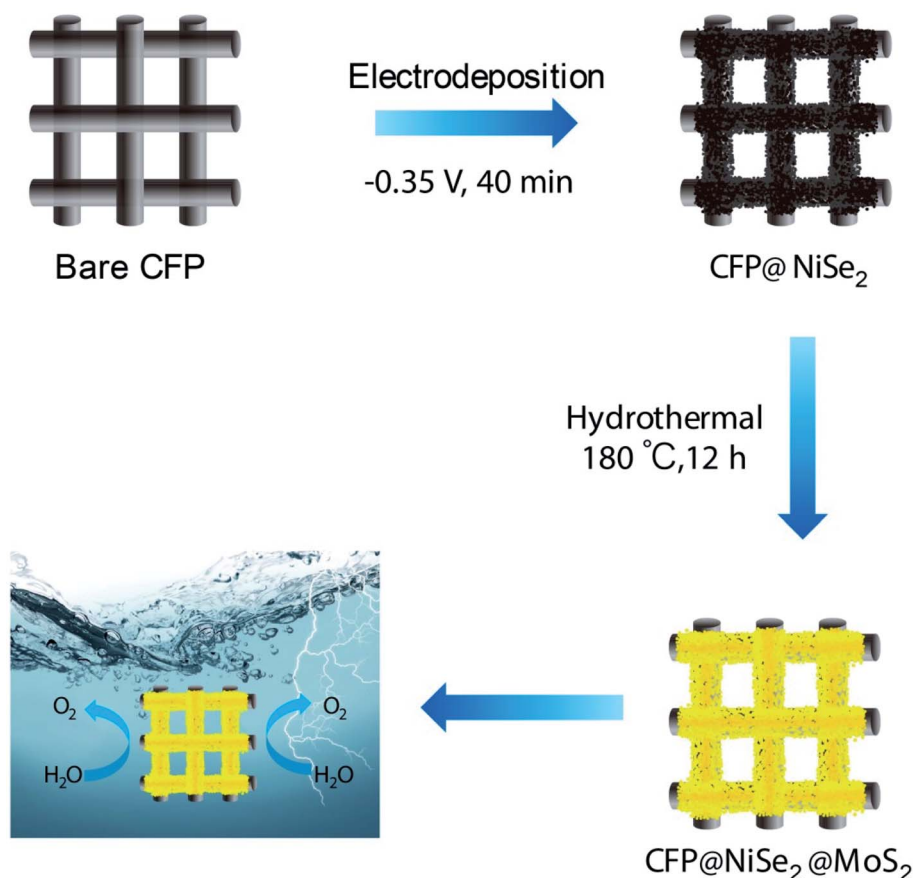


Fig. 1 Construction process of $\text{NiSe}_2\text{@MoS}_2$ nano-heterostructures on CFP.

First, the NiSe_2 film was electrodeposited on a carbon fiber paper (CFP, $1 \times 1 \text{ cm}^2$, TGP-H-60, Toray) by a three-electrode electrochemical cell (CHI660E, CH Instruments). The CFP substrate, a saturated calomel electrode (SCE), and a graphite rod were employed as the working, reference, and counter electrodes, respectively. The electrolyte composed of 100 mL deionized water, 4.45 g $\text{NiCl}_2 \cdot 6\text{H}_2\text{O}$, 1.44 g SeO_2 , and 1.02 g LiCl . The potential was kept at -0.35 V (vs. SCE) for 40 min. Then, the deposited NiSe_2 film (CFP@NiSe_2) was washed using deionized water and dried in a vacuum drying oven at 60°C .

Second, the MoS_2 film was coated on CFP@NiSe_2 by the hydrothermal synthesis. In this process, the amount of precursor and technological conditions are very strict. The precursor solution, including 0.06 g $(\text{NH}_4)_6\text{Mo}_7\text{O}_{24} \cdot 4\text{H}_2\text{O}$, 0.15 g $\text{SC}(\text{NH}_2)_2$, and 30 mL deionized water, was magnetically stirred for 5 min and allowed to stand at 60°C for 1 h. Then, it was transferred into a 50 mL airtight reactor and was allowed to stand at 180°C for 12 h to afford $\text{CFP@NiSe}_2\text{@MoS}_2$. It was washed with deionized water and dried in a vacuum drying oven at 60°C . Detailed procedures refer to ref. 33.

2.2. Characterization

First, the material structure of the obtained samples was observed by various means. The morphology observation was carried out *via* scanning electron microscopy (SEM, S-4800,

Hitachi), high-resolution transmission electron microscopy (HRTEM, TECNAI G2F20, FEI), and X-ray diffraction (XRD, X'Pert3, Panalytical). Before TEM characterization, the samples were ground into powder and transferred to a copper grid. XRD was carried out with $\text{Cu K}\alpha$ radiation ($\lambda = 1.54 \text{ \AA}$) at 40 mA and 45 kV. The chemical elements of samples were observed *via* energy dispersive spectroscopy (EDS, S-4800, Hitachi) and X-ray photoelectron spectroscopy (XPS, Escalab-250Xi, Thermo-fisher). XPS source is $\text{Al K}\alpha$ ($h\nu = 1486.6 \text{ eV}$) with a power of 22.8 W.

Second, the electrocatalytic OER performances of the obtained samples were observed through a three-electrode electrochemical cell that employs Hg/HgO and graphite rod as reference and counter electrodes, respectively, in a 1 M KOH electrolyte solution. Before the measurement, high-purity oxygen was injected into the electrolyte for 20 min to eliminate the interference of oxygen. Then, the oxygen bubbles formed on the electrode surface were dislodged by magnetic stirring during the process of measurement. The potential E_{RHE} was obtained by the equation of $E_{\text{RHE}} = E_{\text{Hg/HgO}} + 0.059\text{pH} + 0.098$. OER polarization curves were obtained by linear sweep voltammetry (LSV) at a scan rate of 10 mV s^{-1} from 0.5 to 2 V (vs. RHE). The result was corrected by the equation of $\eta_{\text{corr}} = \eta_{\text{exp}} - iR$ to eliminate the effect of series resistance. Electrochemical impedance spectra (EIS) were obtained at 1.51 V (vs. RHE) in



a frequency range of 10^5 –0.1 Hz with an amplitude of 5 mV. The double-layer capacitance (C_{dl}), obtained by cyclic voltammetry (CV) tests at different scan rates from 20 to 200 mV s^{-1} in a range of 0.68–0.78 V (vs. RHE), was used to evaluate the electrochemically active surface area (ECSA).

3. Results and discussion

NiSe_2 and MoS_2 films were coated on a CFP substrate, respectively. According to Fig. 2(a–c), rich voids between carbon fibers in the CFP substrate can enlarge the contact of the catalyst to the electrolyte, which are beneficial to improving the OER

activity. According to the enlarged view in the inset, due to the poor crystallinity induced by the low temperature in the constructing process, both NiSe_2 and MoS_2 nanosheets are disorderly distributed in the film. Owing to the disorderly distribution, abundant edges of NiSe_2 and MoS_2 nanosheets can further improve the contact area and activity. Moreover, the close contact between NiSe_2 and CFP obtained by the electrochemical deposition can reduce the charge transfer impedance in the OER process. As shown in Fig. 2(d), the thickness of the $\text{NiSe}_2@\text{MoS}_2$ film is ~ 550 nm. According to further HRTEM observation (Fig. 2(e)), the $\text{NiSe}_2@\text{MoS}_2$ heterostructure is composed of 0.27 nm MoS_2 (002) face and 0.66 nm NiSe_2 (210)

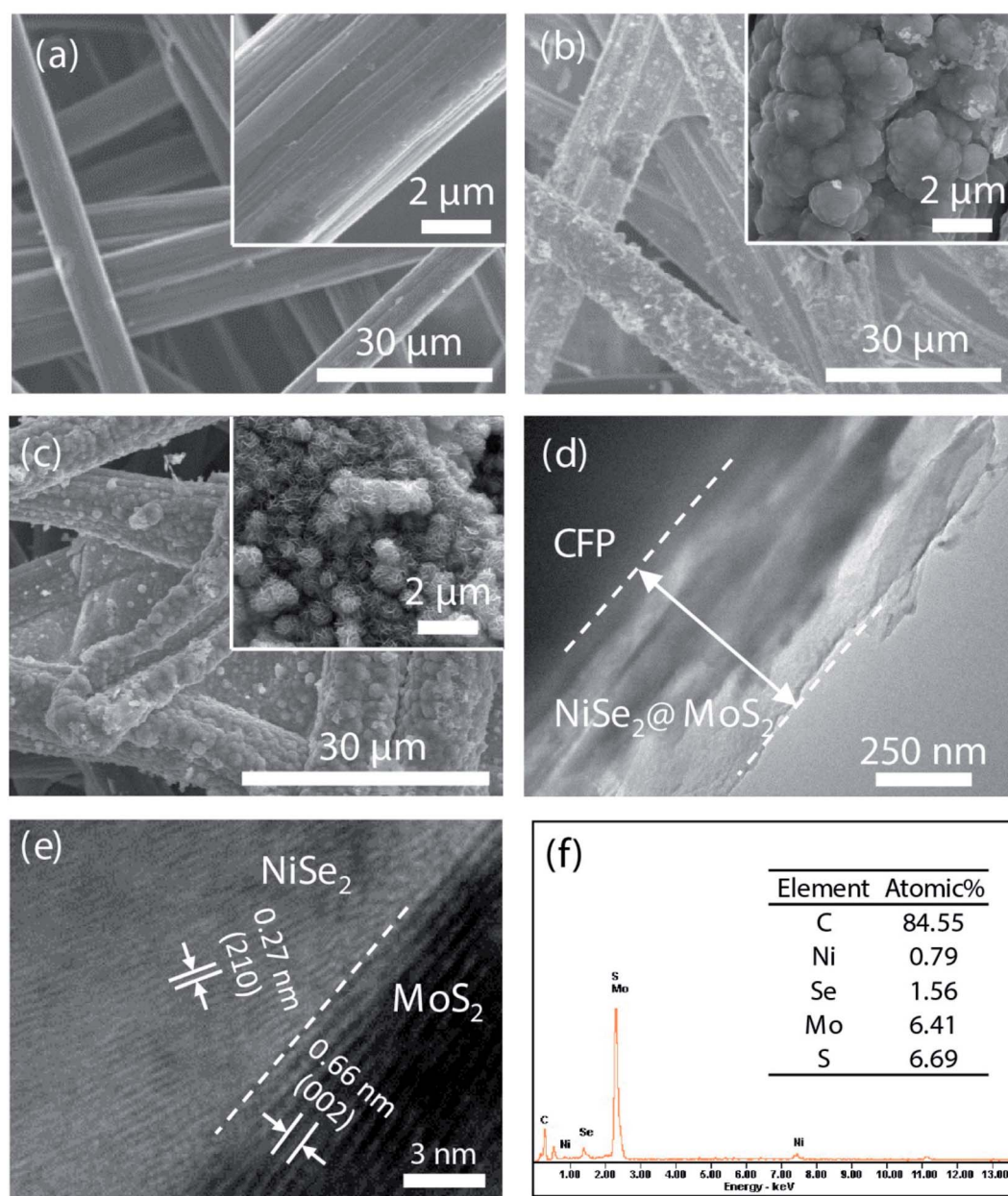


Fig. 2 SEM images of (a) CFP, (b) CFP@NiSe_2 , (c) $\text{CFP@NiSe}_2@\text{MoS}_2$. (d) TEM result of $\text{CFP@NiSe}_2@\text{MoS}_2$. (e) HRTEM result of $\text{NiSe}_2@\text{MoS}_2$. The $\text{NiSe}_2@\text{MoS}_2$ nano-heterostructure composed of MoS_2 (002) and NiSe_2 (210) faces can be clearly observed. (f) EDS results of $\text{CFP@NiSe}_2@\text{MoS}_2$. Ratio of Se/Ni is close to 2, while that of S/Mo is close to 1, indicating that it is sulfur deficient.



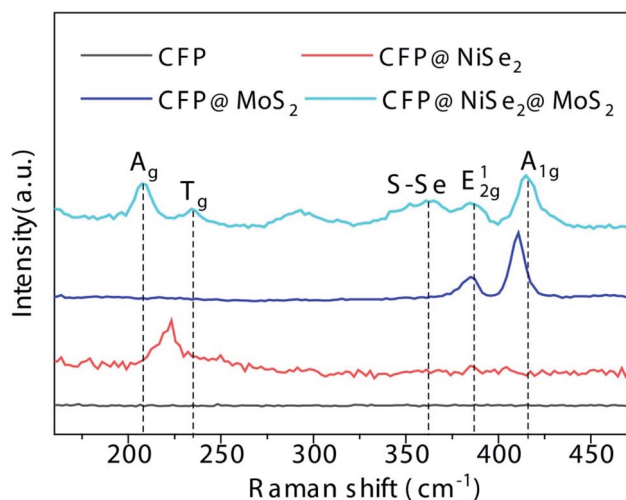


Fig. 3 Raman results of the samples. Peaks A_g and T_g belong to $NiSe_2$, while E_{2g}^1 and A_{1g} belong to MoS_2 . The presence of the peak S–Se confirms that the $NiSe_2@MoS_2$ heterostructure was formed.

face. EDS spectra were further recorded to observe the element composition of the heterostructure (Fig. 2(f)). The ratio of Se/Ni is close to 2 while that of S/Mo is close to 1, indicating that the obtained $NiSe_2@MoS_2$ is sulfur deficient.

As shown in Fig. 3, the samples were further observed by Raman spectroscopy. In the spectrum of $CFP@NiSe_2@MoS_2$, peaks A_g and T_g of $NiSe_2$ are shown at ~ 208 and ~ 235 cm^{-1} , respectively, while E_{2g}^1 and A_{1g} of MoS_2 are shown at ~ 379 and ~ 405 cm^{-1} , respectively, indicating that $NiSe_2@MoS_2$ is indeed deposited on CFP.^{34,35} The interfering peak at ~ 290 cm^{-1} , originating from internal strain of MoS_2 , is caused by the disorder of the grains and defects.³⁶ The S–Se peak at ~ 360 cm^{-1} , originating from S–Se pairs, further confirms that the $NiSe_2@MoS_2$ heterostructure is formed.³⁷ Compared with $CFP@MoS_2$, peaks E_{2g}^1 and A_{1g} of MoS_2 in $CFP@NiSe_2@MoS_2$ exhibit an obvious blue shift, because the crystal symmetry is destroyed by the defects. The defects are from the $NiSe_2$ substrate and $NiSe_2@MoS_2$ heterostructures, which can improve the exposure of active sites and OER activity of MoS_2 .^{38–40} Moreover, peaks A_g and T_g cannot be observed independently in $CFP@NiSe_2$, indicating that the crystallinity of $NiSe_2$ prepared by the electrochemical deposition is relatively low. Then, the crystallinity is improved by the subsequent hydrothermal process of MoS_2 , which helps to reduce the charge transfer impedance in the process of OER.

As shown in Fig. 4, structures of the samples were also observed by XRD. The standard diffraction peaks of $NiSe_2$ and MoS_2 are shown in PDF no. 41-1945 and no. 37-1942, respectively. Peaks at 26.3° and 54.2° originate from the CFP substrate. In the spectra of $CFP@NiSe_2$, peaks corresponding to (200), (210), (211), (220), (311), and (321) planes of $NiSe_2$ are clearly shown at around 29.4° , 33.5° , 36.6° , 43.5° , 50.7° , and 57.5° , respectively.³² According to the spectra of $CFP@MoS_2$, the (002) peak of MoS_2 can be observed at 13.1° . The simultaneous appearance of peaks of $NiSe_2$ and MoS_2 in $CFP@NiSe_2@MoS_2$ further confirms that $NiSe_2$ and MoS_2 are successfully deposited on the

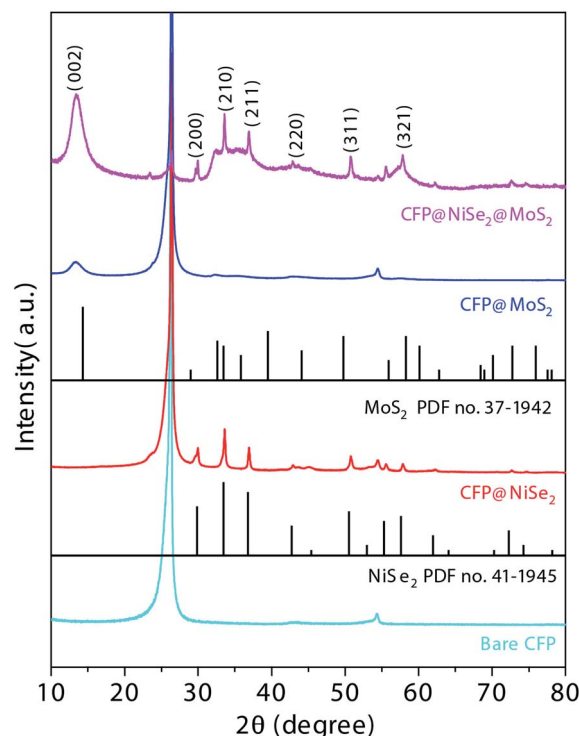


Fig. 4 XRD spectra of the samples. The standard diffraction peaks of $NiSe_2$ and MoS_2 are shown in PDF no. 41-1945 and no. 37-1942 respectively. Peaks (002) of MoS_2 , (200), (210), (211), (220), (311), and (321) of $NiSe_2$ are clearly exhibited.

CFP substrate. Moreover, compared with $CFP@MoS_2$, the (002) peak has a blue shift from 13.1° to 13.5° in $CFP@NiSe_2@MoS_2$ owing to the defects from the $NiSe_2$ substrate and $NiSe_2@MoS_2$ heterostructures. This structure is in favor of the improvement of the OER activity, which is consistent with the Raman results.

The composition of the samples was further analyzed by XPS. According to the spectra of Ni 2p and Se 3d shown in Fig. 5(a and b), peaks of Ni $2p_{1/2}$ and Ni $2p_{3/2}$ belonging to Ni^{4+} of $NiSe_2$ are shown at 870.2 and 853.1 eV with their satellite peaks at 875.7 and 859.2 eV, respectively.⁴¹ Peaks of Se $3d_{3/2}$ and Se $3d_{5/2}$ at 53.5 and 52.7 eV, respectively, belong to Se_2^{2-} of $NiSe_2$, while an oxidized Se peak is shown at 57 eV.⁴² Moreover, as shown in Fig. 5(c and d), peaks of Mo $3d_{3/2}$ and Mo $3d_{5/2}$ at 231.2 and 228 eV are attributed to Mo^{4+} of MoS_2 , and the peak at 225.5 eV is due to the Mo–S bond. Peaks of S $2p_{1/2}$ and S $2p_{3/2}$ at 161.8 and 160.8 eV are due to S_2^{2-} of MoS_2 .⁴³ Therefore, $NiSe_2$ and MoS_2 have been deposited on CFP successfully. In addition, compared with $CFP@NiSe_2$ and $CFP@MoS_2$, peaks of Ni 2p and Se 3d show a negative shift, while those of Mo 3d and S 2p have a positive shift in $CFP@NiSe_2@MoS_2$, further confirming that the $NiSe_2@MoS_2$ heterostructure has been formed.⁴⁴ The Mo-to-S ratio also needs to be observed because OER active sites of MoS_2 have been shown at its edge with S-vacancies.²¹ According to the peaks of Mo 3d and S 2p shown in Fig. 5(c and d), compared with $CFP@MoS_2$, the Mo/S ratio increases from 0.81 to 0.93 in $CFP@NiSe_2@MoS_2$, indicating that S-vacancies increase by about 15% in the latter. Thus, the obtained $NiSe_2@MoS_2$ can expose more active sites and improve the OER activity.



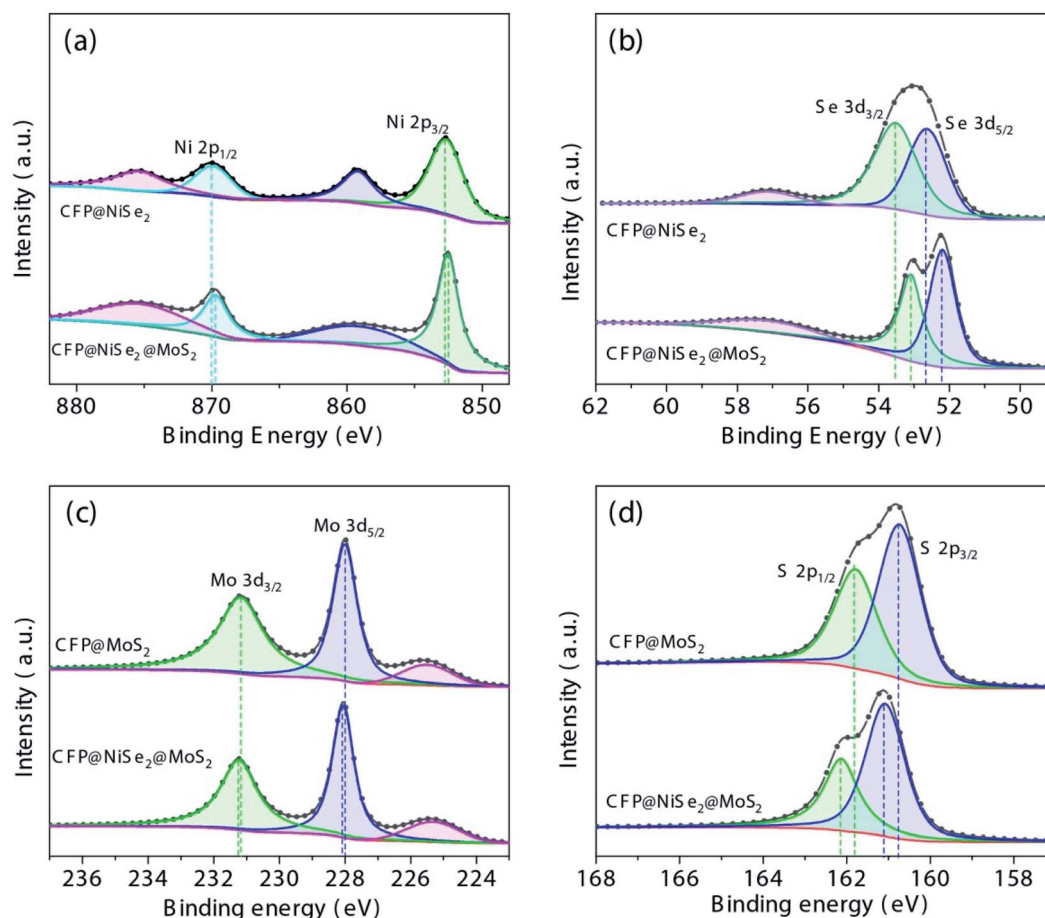


Fig. 5 XPS spectra of (a) Ni 2p, (b) Se 3d, (c) Mo 3d, and (d) S 2p.

The electrocatalytic OER performances of the samples were evaluated by various electrochemical measurements. The OER polarization curves obtained by LSV in 1 M KOH solution are shown in Fig. 6(a). Unsurprisingly, the bare CFP with an almost zero current density shows no electrocatalytic OER activity in the potential window from 1.2 to 1.7 V (vs. RHE). For CFP@MoS₂, the potential driving the current density of 10 mA cm⁻² needs 1.62 V (vs. RHE), which indicates an overpotential η_{10} of 390 mV. Although it has some reduction than CFP, it is still relatively high and worthless as an OER catalyst. In the curve of CFP@NiSe₂, the peak at ~1.36 V (vs. RHE) is attributed to the oxidation of Ni.^{32,45} It was first oxidized to Ni(OH)₂, which proceeded as $\text{Ni} + 2\text{OH}^- \rightarrow \text{Ni(OH)}_2 + 2\text{e}^-$. As the potential increased, Ni(OH)₂ was further oxidized to NiOOH, which proceeded as $\text{Ni(OH)}_2 + \text{OH}^- \rightarrow \text{NiOOH} + \text{H}_2\text{O} + \text{e}^-$. The overpotential η_{10} of 290 mV is lower than that of CFP@MoS₂. When the current density increases to 20 mA cm⁻², the overpotential η_{20} of 356 mV is also lower than that of CFP@MoS₂ (440 mV), indicating a better activity. However, it is not the best. Obviously, CFP@NiSe₂@MoS₂ with η_{10} of 267 mV and η_{20} of 320 mV exhibits the highest catalytic performance.

Tafel slopes of the samples were further observed by fitting the polarization curves with the Tafel equation ($\eta = a + b \log j$, where b is the Tafel slope). According to Fig. 6(b) and Table 1,

Tafel slopes of the samples are 159, 112, and 85 mV dec⁻¹, respectively. The much smaller Tafel slope of CFP@NiSe₂@MoS₂ further confirms its excellent OER catalytic performance. It is also compared with that of other MoS₂-based and noble metal oxide electro-catalysts reported recently (Table 2). CFP@MoS₂ with η_{10} of 390 mV and b of 159 mV dec⁻¹ shows an obvious activity improvement than the exfoliated MoS₂, which can be attributed to the more exposure of active sites induced by the small grain.²³ Compared with CFP@MoS₂, the performance of CFP@NiSe₂@MoS₂ has a further improvement. Moreover, the performance of CFP@NiSe₂@MoS₂ and MoS₂/Ni₃S₂ is similar. However, compared to the dependence of MoS₂/Ni₃S₂ on nickel foam, NiSe₂@MoS₂ can be deposited on the surface of any conductor as shown in this study, which greatly expands its application.²⁷ Compared with that of Co₃S₄@MoS₂, CoS₂-C@MoS₂, Co₃O₄@MoS₂/CC, and RuO₂, although the Tafel slope of CFP@NiSe₂@MoS₂ is bigger, it has a smaller overpotential η_{10} , indicating that CFP@NiSe₂@MoS₂ is an excellent OER electro-catalyst and worth exploring as a substitute for noble metal-based materials.

As shown in Fig. 6(c), electrochemical impedance spectra (EIS) of the samples were measured and fitted by the equivalent circuit (Fig. 6(d)), where R_s is the series resistance, R_{ct} is the charge-transfer resistance, and CPE is the constant phase



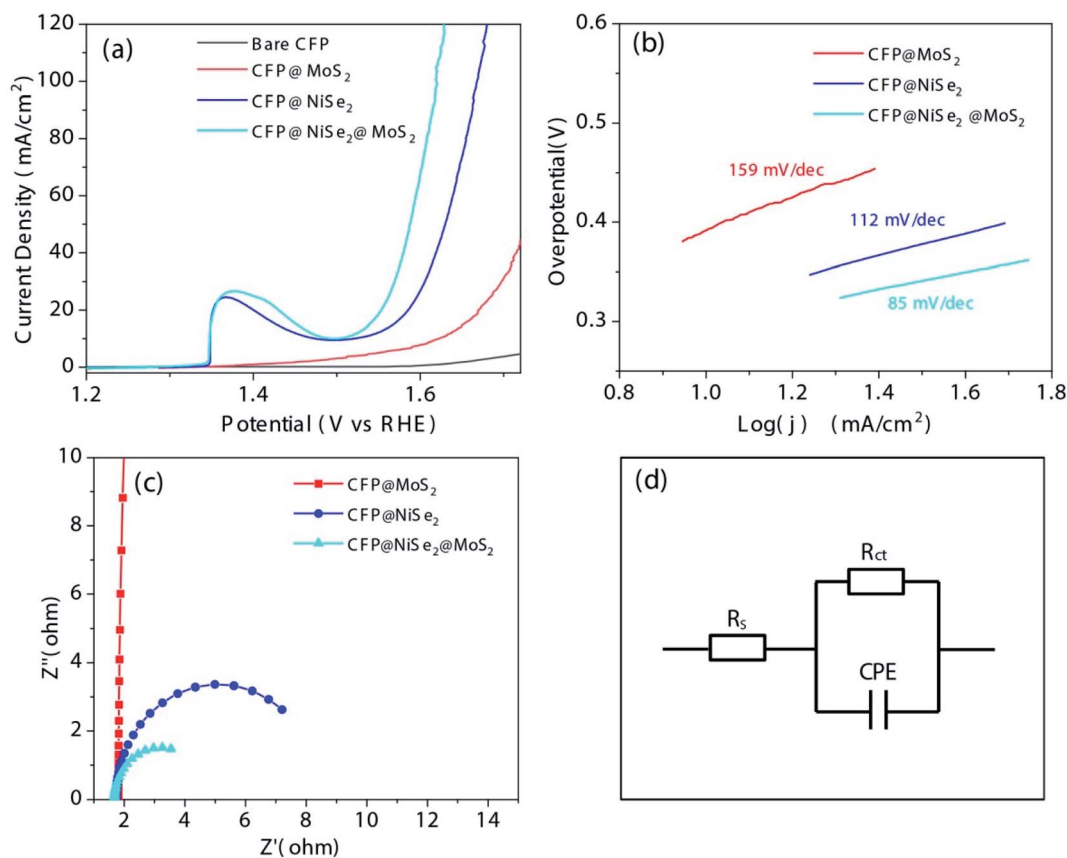


Fig. 6 (a) OER polarization curves, (b) Tafel plots, and (c) impedance analysis of the samples. (d) The equivalent circuit: R_s is the series resistance, R_{ct} is the charge-transfer resistance, and CPE is the constant phase elements.

elements. According to Fig. 6(c) and Table 3, R_s and R_{ct} of the samples are 1.81 and 567.6, 1.71 and 6.74, 1.68 and 3.03 Ω , respectively. It can be obtained that R_s values of the samples are

Table 1 Overpotential and Tafel slope of the obtained samples

Catalyst	Overpotential η_{10} (mV)	Overpotential η_{20} (mV)	Tafel slope b (mV dec ⁻¹)
CFP@NiSe ₂ @MoS ₂	267	320	85
CFP@NiSe ₂	290	356	112
CFP@MoS ₂	390	440	159

Table 2 The electrocatalytic OER performances of CFP@NiSe₂@MoS₂ and other MoS₂-based electro-catalysts

Catalyst	Tafel slope b (mV dec ⁻¹)	Overpotential η_{10} (mV)	Ref.
CFP@NiSe ₂ @MoS ₂	85	267	This work
CFP@MoS ₂	159	390	This work
Exfoliated MoS ₂	322	420	46
Co ₉ S ₈ @MoS ₂	94	342	25
Co ₃ S ₄ @MoS ₂	43	280	47
CoS ₂ -C@MoS ₂	46	391	26
MoS ₂ /Ni ₃ S ₂	88	218	27
Co ₃ O ₄ @MoS ₂ /CC	58	360	48
RuO ₂	65	380	49

slightly different. However, the R_{ct} value has a significant decrease from 567.6 to 3.03 Ω , which indicates that CFP@NiSe₂@MoS₂ can substantially improve the OER activity.

C_{dl} was used to evaluate ECSA of the samples. As shown in Fig. 7(a–c), CV tests of the samples were performed with different scan rates from 20 to 200 mV s⁻¹ in the regions of non-faradaic potentials (0.68–0.78 V (vs. RHE)). Current density differences between anodic and cathodic *versus* the scanning rate at 0.73 V a (vs. RHE) are shown in Fig. 7(d). Fitting these data linearly can obtain the C_{dl} value. According to Fig. 7(d) and Table 3, C_{dl} values of the samples are 0.78, 4.64, and 6.25 mF cm⁻², respectively. The much larger C_{dl} of CFP@NiSe₂@MoS₂ among the samples indicates that the ECSA was significantly increased. Hence, the outstanding OER performance of CFP@NiSe₂@MoS₂ is not only due to the faster electron transfer rate but also due to the increasing ECSA.

Table 3 Series resistance R_s , charge-transfer resistance R_{ct} , and double-layer capacitance C_{dl} of the obtained samples

Catalyst	Resistance R_s (Ω)	Resistance R_{ct} (Ω)	C_{dl} (mF cm ⁻²)
CFP@NiSe ₂ @MoS ₂	1.68	3.03	0.78
CFP@NiSe ₂	1.71	6.74	4.64
CFP@MoS ₂	1.81	567.6	6.25

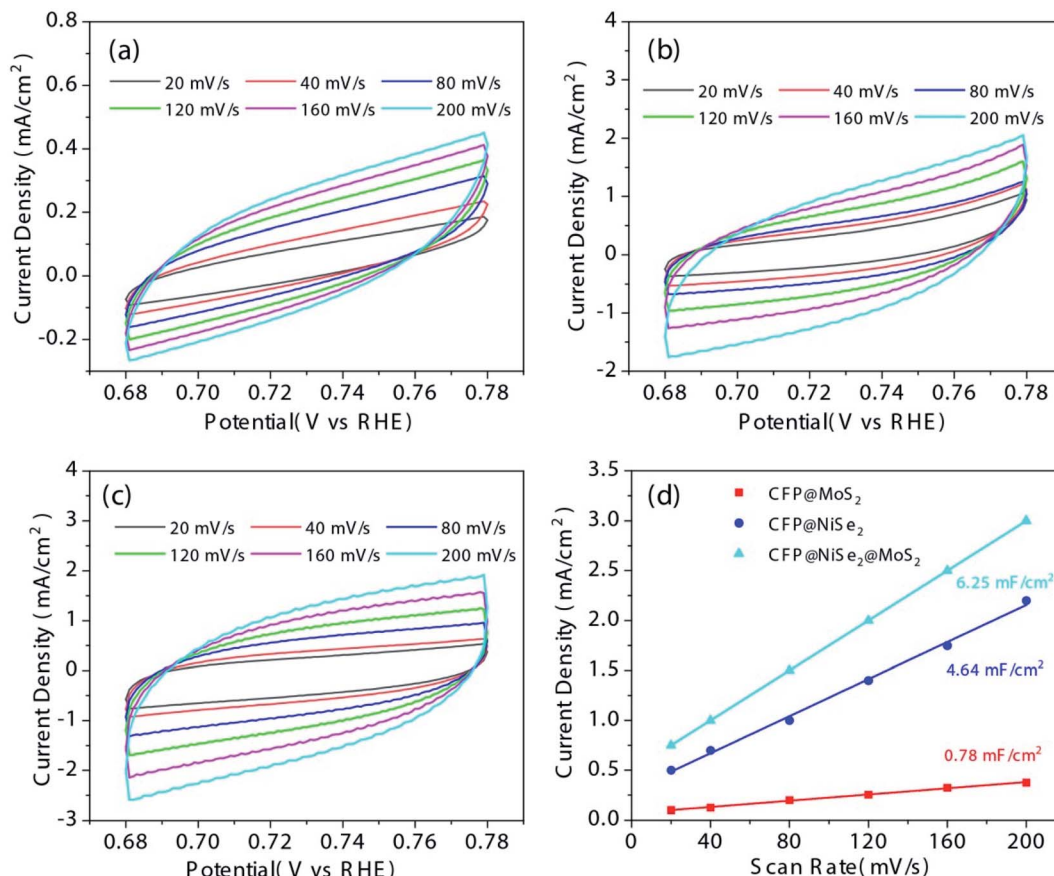


Fig. 7 CV tests of (a) CFP@MoS₂, (b) CFP@NiSe₂, and (c) CFP@NiSe₂@MoS₂ with different scan rates from 20 to 200 mV s⁻¹ in a range of 0.68–0.78 V (vs. RHE). (d) Current density difference between anodic and cathodic *versus* the scanning rate at 0.73 V (vs. RHE). C_{dl} obtained by linear fitting the data was used to evaluate ECSA of the samples because C_{dl} was proportional to ECSA.

The durability of CFP@NiSe₂@MoS₂ was further measured by repeating the CV test for 1000 cycles. According to Fig. 8(a), the difference in current density is negligible before and after 1000 cycles. The current density *versus* time under a constant overpotential of 340 mV is shown in Fig. 8(b). Only 6% loss after 10 h indicates its outstanding durability.

The mechanism that NiSe₂@MoS₂ has a better catalytic performance than pure MoS₂ or NiSe₂ can be summarized as follows:

(1) The disordered NiSe₂ increases the contact area between MoS₂ and the electrolyte solution. NiSe₂@MoS₂ samples are obtained by depositing MoS₂ on NiSe₂, while pure MoS₂ and NiSe₂ are deposited directly on the bare CFP substrate. Compared with the smooth bare CFP substrate, the disordered distribution of NiSe₂ nanosheets (as shown in Fig. 2) can further increase the superficial area of MoS₂, so as to increase the contact area between MoS₂ and the electrolyte solution. This is an effective way to improve the OER efficiency of MoS₂.

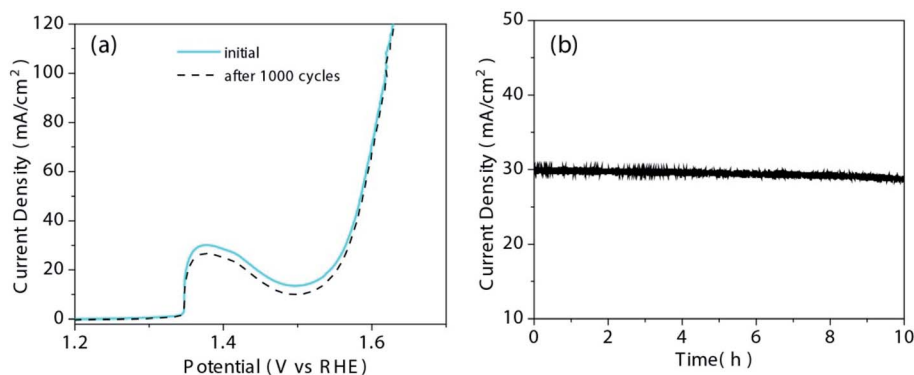


Fig. 8 (a) Durability measurement of CFP@NiSe₂@MoS₂. Difference in current density is negligible before and after 1000 cycles. (b) The current density *versus* time under a constant overpotential of 340 mV.



According to the C_{dl} results (as shown in Fig. 7), the ECSA of $NiSe_2@MoS_2$ significantly increased than that of pure $NiSe_2$ and MoS_2 .

(2) The hybridization of $NiSe_2$ increases the defects of MoS_2 , which can improve the exposure of active sites and OER activity of MoS_2 . It has been demonstrated that defects such as doping, atomic vacancy and lattice distortion can increase the exposure of active sites of MoS_2 .^{38–40} According to the results of the material characterization, the defects of MoS_2 do increase in $NiSe_2@MoS_2$. As shown in the Raman results (Fig. 3), some phenomena in $NiSe_2@MoS_2$ such as the appearance of the interfering peak at $\sim 290\text{ cm}^{-1}$, the blue shift and expansion of the characteristic peak of MoS_2 , indicate that the crystal symmetry of MoS_2 was damaged by the defects.

According to the XPS results (Fig. 5), the $\sim 15\%$ increase of S-vacancies in $NiSe_2@MoS_2$ confirms that the hybridization of $NiSe_2$ increases the exposure of active sites of MoS_2 .

(3) Doping Ni atoms into MoS_2 at the interface of the $NiSe_2@MoS_2$ heterostructure can effectively reduce the kinetic energy barrier of the initial water-dissociation step and facilitate the desorption of $-OH$,²⁷ so as to improve the OER performance. According to Raman and XPS results (Fig. 3 and 5), it can be confirmed that the chemical bonds between $NiSe_2$ and MoS_2 are generated at the interface of the $NiSe_2@MoS_2$ heterostructure.

4. Conclusion

In summary, the novel $NiSe_2@MoS_2$ nano-heterostructure for electrocatalytic OER has been constructed on a CFP substrate by a simple method. The electrocatalytic OER performances were fully evaluated by electrochemical measurements and further compared with that of other MoS_2 -based and noble metal oxide electro-catalysts. It exhibits an outstanding catalytic performance with an overpotential η_{20} of 323 mV and a Tafel slope of 85 mV dec^{-1} . Just 6% loss of current density before and after 10 h also indicates its excellent durability. Therefore, it is an excellent OER electro-catalyst and worth exploring as a substitute for noble metal-based materials.

Author contributions

Yazhou Huang: resources, conceptualization, methodology, investigation, writing – original draft, writing – review & editing. Jiacai Huang: writing – review & editing, methodology, formal analysis. Kunshan Xu: methodology, data curation. Ranran Geng: validation, formal analysis.

Conflicts of interest

There are no conflicts to declare.

Acknowledgements

This work was supported by the National Natural Science Foundation of China (51905259), the Natural Science Foundation of Jiangsu Province (BK20191017), the Natural Science Research Program for Higher Education of Jiangsu Province

(19KJB460003, 20KJA510007), the Scientific Research Fund of Nanjing Institute of Technology (YKJ201859).

References

- 1 M. S. Dresselhaus and I. L. Thomas, *Nature*, 2001, **414**, 332–337.
- 2 A. Yamaguchi, R. Inuzuka, T. Takashima, T. Hayashi, K. Hashimoto and R. Nakamura, *Nat. Commun.*, 2014, **5**, 4256.
- 3 L. Gao, X. Cui, Z. Wang, C. D. Sewell, Z. Li, S. Liang, M. Zhang, J. Li, Y. Hu and Z. Lin, *Proc. Natl. Acad. Sci. U. S. A.*, 2021, **118**, e2023421118.
- 4 G. Liao, J. Fang, Q. Li, S. Li, Z. Xu and B. Fang, *Nanoscale*, 2019, **11**, 7062–7096.
- 5 Y. Zhang, X. Wang, F. Luo, Y. Tan, L. Zeng, B. Fang and A. Liu, *Appl. Catal., B*, 2019, **256**, 117852.
- 6 S. Shen, Z. Lin, K. Song, Z. Wang, L. Huang, L. Yan, F. Meng, Q. Zhang, L. Gu and W. Zhong, *Angew. Chem., Int. Ed.*, 2021, **60**, 12360–12365.
- 7 Z. Lin, S. Shen, Z. Wang and W. Zhong, *iScience*, 2021, **24**, 102469.
- 8 C. C. Mccrory, S. Jung, J. C. Peters and T. F. Jaramillo, *J. Am. Chem. Soc.*, 2013, **135**, 16977–19687.
- 9 J. Wang, W. Cui, Q. Liu, Z. Xing, A. M. Asiri and X. Sun, *Adv. Mater.*, 2016, **28**, 215–230.
- 10 W. Zhong, Z. Lin, S. Feng, D. Wang, S. Shen, Q. Zhang, L. Gu, Z. Wang and B. Fang, *Nanoscale*, 2019, **11**, 4407–4413.
- 11 L. Xu, Z. Wang, J. Wang, Z. Xiao, X. Huang, Z. Liu and S. Wang, *Nanotechnology*, 2017, **28**, 165402.
- 12 H. Li, Y. Shao, Y. Su, Y. Gao and X. Wang, *Chem. Mater.*, 2016, **28**, 1155–1164.
- 13 J. R. Swierk, S. Klaus, L. Trotochaud, A. T. Bell and T. D. Tilley, *J. Phys. Chem. C*, 2015, **119**, 19022–19029.
- 14 T. Chun, C. Ningyan, P. Zonghua, X. Wei and S. Xuping, *Angew. Chem., Int. Ed.*, 2015, **54**, 9351–9355.
- 15 L. Feng, F. Song and X. Hu, *Energy Environ. Sci.*, 2015, **8**, 2347–2351.
- 16 X. Cui, S. Lei, A. C. Wang, L. Gao, Q. Zhang, Y. Yang and Z. Lin, *Nano Energy*, 2020, **70**, 104525.
- 17 A. Xu, W. Tu, S. Shen, Z. Lin, N. Gao and W. Zhong, *Appl. Surf. Sci.*, 2020, **528**, 146949.
- 18 Z. Wang, Z. Lin, J. Deng, S. Shen, F. Meng, J. Zhang, Q. Zhang, W. Zhong and L. Gu, *Adv. Energy Mater.*, 2021, **11**, 2003023.
- 19 Y. Yan, B. Y. Xia, Z. Xu and X. Wang, *ACS Catal.*, 2014, **4**, 1693–1705.
- 20 J. D. Benck, Z. B. Chen, L. Y. Kuritzky, A. J. Forman and T. F. Jaramillo, *ACS Catal.*, 2012, **2**, 1916–1923.
- 21 B. Mohanty, M. Ghorbani-Asl, S. Kretschmer, A. Ghosh, P. Guha, S. K. Panda, B. Jena, A. V. Krashennnikov and B. K. Jena, *ACS Catal.*, 2018, **8**, 1683–1689.
- 22 D. Xiong, Q. Zhang, W. Li, J. Li, X. Fu, M. F. Cerqueira, P. Alpuim and L. Liu, *Nanoscale*, 2017, **9**, 2711–2717.
- 23 Y. Huang, L. Liu and X. Liu, *Nanotechnology*, 2019, **30**, 095402.



- 24 H. Zhu, J. Zhang, R. Yanzhang, M. Du, Q. Wang, G. Gao, J. Wu, G. Wu, M. Zhang, B. Liu, J. Yao and X. Zhang, *Adv. Mater.*, 2015, **27**, 4752–4759.
- 25 J. Bai, T. Meng, D. Guo, S. Wang, B. Mao and M. Cao, *ACS Appl. Mater. Interfaces*, 2018, **10**, 1678–1689.
- 26 Y. Zhu, L. Song, N. Song, M. Li, C. Wang and X. Lu, *ACS Sustainable Chem. Eng.*, 2019, **7**, 2899–2905.
- 27 J. Zhang, T. Wang, D. Pohl, B. Rellinghaus, R. Dong, S. Liu, X. Zhuang and X. Feng, *Angew. Chem.*, 2016, **128**, 6814–6819.
- 28 X. Zhao, Y. Yang, Y. Li, X. Cui, Y. Zhang and P. Xiao, *J. Mater. Sci.*, 2016, **51**, 3724–3734.
- 29 W. Zhong, Z. Wang, N. Gao, L. Huang, Z. Lin, Y. Liu, F. Meng, J. Deng, S. Jin, Q. Zhang and L. Gu, *Angew. Chem., Int. Ed.*, 2020, **59**, 22743–22748.
- 30 W. Zhong, B. Xiao, Z. Lin, Z. Wang, L. Huang, S. Shen, Q. Zhang and L. Gu, *Adv. Mater.*, 2021, **33**, 2007894.
- 31 Z. Lin, B. Xiao, Z. Wang, W. Tao, S. Shen, L. Huang, J. Zhang, F. Meng, Q. Zhang, L. Gu and W. Zhong, *Adv. Funct. Mater.*, 2021, 2102321.
- 32 J. Zhu and Y. Ni, *CrystEngComm*, 2018, **20**, 3344–3352.
- 33 Y. Huang, J. Lv, J. Huang, K. Xu and L. Liu, *Nanotechnology*, 2021, **32**, 175602.
- 34 F. Wang, Y. Li, T. A. Shifa, K. Liu, F. Wang, Z. Wang, P. Xu, Q. Wang and J. He, *Angew. Chem., Int. Ed.*, 2016, **55**, 6919–6924.
- 35 L. Liu, Y. Huang, J. Sha and Y. Chen, *Nanotechnology*, 2017, **28**, 195605.
- 36 Z. Jin, S. Shin, D. H. Kwon, S.-J. Han and Y.-S. Min, *Nanoscale*, 2014, **6**, 14453–14458.
- 37 C. d. l. Heras and F. Agulló-Rueda, *J. Phys.: Condens. Matter*, 2000, **12**, 5317–5324.
- 38 J. Xie, H. Zhang, S. Li, R. Wang, X. Sun, M. Zhou, J. Zhou, X. W. Lou and Y. Xie, *Adv. Mater.*, 2013, **25**, 5807–5813.
- 39 H. Li, C. Tsai, A. L. Koh, L. Cai, A. W. Contryman, A. H. Fragapane, J. Zhao, H. S. Han, H. C. Manoharan, F. Abild-Pedersen, J. K. Nørskov and X. Zheng, *Nat. Mater.*, 2016, **15**, 48–53.
- 40 J. Zhang, X. Xu, L. Yang, D. Cheng and D. Cao, *Small Methods*, 2019, **3**, 1900653.
- 41 I. H. Kwak, H. S. Im, D. M. Jang, Y. W. Kim, K. Park, Y. R. Lim, E. H. Cha and J. Park, *ACS Appl. Mater. Interfaces*, 2016, **8**, 5327–5334.
- 42 J. Liang, Y. Yang, J. Zhang, J. Wu, P. Dong, J. Yuan, G. Zhang and J. Lou, *Nanoscale*, 2015, **7**, 14813–14816.
- 43 L. Liu, X. Liu and S. Jiao, *J. Colloid Interface Sci.*, 2020, **564**, 77–87.
- 44 S. Li, W. Zang, X. Liu, S. J. Pennycook, Z. Kou, C. Yang, C. Guan and J. Wang, *Chem. Eng. J.*, 2019, **359**, 1419–1426.
- 45 M. W. Louie and A. T. Bell, *J. Am. Chem. Soc.*, 2013, **135**, 12329–12337.
- 46 J. Wu, M. Liu, K. Chatterjee, K. P. Hackenberg, J. Shen, X. Zou, Y. Yan, J. Gu, Y. Yang, J. Lou and P. M. Ajayan, *Adv. Mater. Interfaces*, 2016, **3**, 1500669.
- 47 Y. Guo, J. Tang, Z. Wang, Y.-M. Kang, Y. Bando and Y. Yamauchi, *Nano Energy*, 2018, **47**, 494–502.
- 48 J. Liu, J. Wang, B. Zhang, Y. Ruan, H. Wan, X. Ji, K. Xu, D. Zha, L. Miao and J. Jiang, *J. Mater. Chem. A*, 2018, **6**, 2067–2072.
- 49 S. Jung, C. C. L. McCrory, I. M. Ferrer, J. C. Peters and T. F. Jaramillo, *J. Mater. Chem. A*, 2016, **4**, 3068–3076.

